Large-scale flow and Reynolds numbers in the presence of boiling in locally heated turbulent convection

Paul B. J. Hoefnagels,[1,2] Ping Wei,[3] Daniela Narezo Guzman,[1,2] Chao Sun,[1,4] Detlef Lohse,[1,5] and Guenter Ahlers[2]

[1]*Physics of Fluids Group, Department of Science and Technology, J.M. Burgers Center for Fluid Dynamics, Mesa⁺-Institute, and Max Planck Center Twente, University of Twente, P.O. Box 217, 7500 AE Enschede, The Netherlands*

[2]*Department of Physics, University of California, Santa Barbara, CA 93106, USA*

[3]*School of Aerospace Engineering and Applied Mechanics, Tongji University, Shanghai, China*

[4]*Center for Combustion Energy and Department of Thermal Engineering, Tsinghua University, Beijing 100084, China*

[5]*Max Planck Institute for Dynamics and Self-Organization, Am Fassberg 17, 37077 Göttingen, Germany*

(Received 9 December 2016; published 27 July 2017)

We report on an experimental study of the large-scale flow (LSF) and Reynolds numbers in turbulent convection in a cylindrical sample with height equal to its diameter and heated locally around the center of its bottom plate (locally heated convection). The sample size and shape are the same as those of Narezo Guzman *et al.* [D. Narezo Guzman *et al.*, J. Fluid Mech. **787**, 331 (2015); **795**, 60 (2016)]. Measurements are made at a nearly constant Rayleigh number as a function of the mean temperature, both in the presence of controlled boiling (two-phase flow) and for the superheated fluid (one-phase flow). Superheat values $T_b - T_{on}$ up to about 11 K (T_b is the bottom-plate temperature and T_{on} is the lowest T_b at which boiling is observed) are used. The LSF is less organized than it is in (uniformly heated) Rayleigh-Bénard convection (RBC), where it takes the form of a single convection roll. Large-scale-flow-induced sinusoidal azimuthal temperature variations (like those found for RBC) could be detected only in the lower portion of the sample, indicating a less organized flow in the upper portions. Reynolds numbers are determined using the elliptic model (EM) of He and Zhang [G.-W. He and J.-B. Zhang, Phys. Rev. E **73**, 055303(R) (2006)]. We found that for our system the EM is applicable over a wide range of space and time displacements, as long as these displacements are within the inertial range of the temporal and spatial spectrum. At three locations in the sample the results show that the vertical mean-flow velocity component is reduced while the fluctuation velocity is enhanced by the bubbles of the two-phase flow. Enhancements of velocity fluctuations up to about 60% are found at the largest superheat values. Local temperature measurements within the sample reveal temperature oscillations that also used to determine a Reynolds number. These results are generally consistent with the mean-flow EM results and show a two-phase-flow enhancement of up to about 30%.

DOI: 10.1103/PhysRevFluids.2.074604

I. INTRODUCTION

Boiling usually involves the process of heterogeneous vapor-bubble nucleation, where the bubble formation in a heated liquid is initiated by microscopic foreign objects such as suspended dust particles or by chemical or geometric inhomogeneities at the heated surface. Here we are concerned with boiling in a liquid contained between two parallel horizontal plates, with the lower one heated to a temperature T_b above a characteristic temperature T_{on} where vapor-bubble formation first starts when nucleation centers are present. The upper surface was cooled to T_t well below T_{on}. In the absence of boiling this system is well known as Rayleigh-Bénard convection (RBC), where the fluid undergoes vigorous turbulent one-phase flow (for a general introduction to RBC see, e.g., [1] or [2]; for more detailed reviews see, e.g., [3–5]).

In RBC a large-scale circulation (LSC) (see, e.g., [6–10]) coexists with intense smaller-scale fluctuations of the temperature and the velocity. In the case of samples with nearly equal horizontal and vertical size the LSC takes the form of a single convection roll, with upflow and downflow on opposite sides of the sample near the sidewall. The dynamics of the LSC is driven by the smaller-scale fluctuations and thus the LSC amplitude and azimuthal orientation θ_0 vary irregularly in time [11–15]. The time-averaged temperature in the interior (bulk) of the fluid varies only weakly with vertical and horizontal position [16–22] and two boundary layers (BLs), one below the top plate and the other above the bottom plate, sustain most of the applied temperature difference [23–26]. Hot thermal plumes emanate from the bottom BL and cold ones emerge from the top BL. They are carried by and by virtue of their buoyancy in turn drive the LSC [3,4,27].

In a recent study it was found that the excess heat transport due to the formation of liquid droplets ("rain") under a solid top plate confining a RBC sample of vapor was very reproducible [28]. For this and other reasons the authors concluded that the droplet formation occurred via homogeneous nucleation in the top BL and did not involve nucleation centers on the top surface *per se*. In contrast, the same study showed that boiling over the heated bottom plate of a RBC sample of liquid was very *irreproducible* and initiated by heterogeneous nucleation. The irreproducibility is attributable to the uncontrolled microscopic nature of the roughness of the macroscopically smooth top surface of the bottom plate. The irreproducibility of heterogeneous nucleation interferes with a systematic quantitative study of the boiling process.

The irreproducibility problem mentioned above was overcome recently by Narezo Guzman *et al.* (NG) [29,30]. The top surface of the bottom plate of their sample was that of a thin silicon wafer. Etched into the wafer was a triangular lattice of cylindrical holes that were 100 μm deep and had a diameter of 30 μm. The holes, when filled with vapor while the sample above them was almost entirely liquid, acted as reproducible nucleation centers of vapor bubbles. When the holes were filled with liquid, no nucleation took place and the superheated one-phase RBC flow could be studied for comparison with the same externally applied parameters such as the excess bottom-plate temperature $T_b - T_{on}$ (known as the superheat) and the temperature difference $\Delta T = T_b - T_t$ across the sample.

Initial experiments by NG [29] with a silicon wafer supported and heated over its entire area by a copper plate revealed that nucleation took place also at the corner where the sidewall meets the bottom plate (see Fig. 1 below). For this reason the authors then used a composite bottom plate. It consisted of a 10-cm-diam silicon wafer, but only the central circular area of 2.54 cm diameter was supported by a copper anvil where heat was applied to the sample. This system differs significantly from RBC where the entire bottom plate is heated and we will refer to it as locally heated convection (LHC). Since only the center of the bottom plate is heated, the corresponding conductive heat flux of the LHC cell is different from that of the classical RBC system [29,30]. The lattice of nucleation centers extended only over the heated central area. The remainder of the wafer was supported on its underside by a plastic disk that reached from the anvil to the sidewall. The low conductivity of the plastic allowed a horizontal temperature gradient to develop in the bottom plate. Thus, the junction of the bottom plate and the sidewall was well below T_{on} and did not lead to nucleation even when the 2.54-cm-diam central area was well above T_{on}. The high conductivity of the supporting copper anvil allowed nucleation at a controlled nearly uniform temperature. The excess heat transport [29] due to boiling was measured as a function of the superheat and of the nucleation-center lattice spacing, and many aspects of the bubble nucleation and dynamics [30] were studied using high-speed videography.

One of the conclusions of NG [30] was that the large-scale flow (LSF) in LHC differs in a major way from that in RBC and that it is significantly enhanced by the buoyancy of the rising bubbles. Much of the heat-transport enhancement due to boiling was found to be due to this enhanced flow with only a relatively small fraction due to the latent heat carried by the bubbles. In the present paper we report on a study in the presence and absence of boiling for the same sample geometry as that used by NG. However, our sample contained a much larger number of local temperature probes that enabled us to obtain information about the LSF structure and about the local mean-flow velocity U [see Eq. (5) below] and fluctuation velocity V [Eq. (7) below] and their corresponding Reynolds numbers [Eqs. (6) and (8) below].

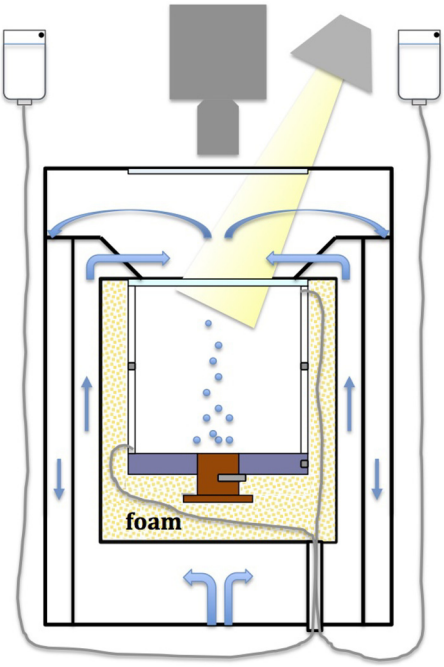

FIG. 1. Schematic drawing of the apparatus.

The system parameters and experimental details are provided in Secs. II and III, respectively. Local temperature measurements were made at ten locations within the bulk of the sample (see Table I). The corresponding temperature autocorrelation and cross-correlation functions were used to obtain local values of U and V using the predictions of the elliptic approximation (EA) of He and Zhang [31] (for a recent review see Ref. [32]) and the assumption that temperature behaves as a passive scalar [33,34] and exhibits self-similarity scaling in the inertial range [35]. We discuss the application of the EA results to our data and summarize the EA predictions [31,36–38] relevant to our work in Sec. IV.

TABLE I. Identifiers ID and the radial and vertical locations of the internal thermistors in cell B. The sample height is $L = 88.3$ mm and the radius is $R = 44.13$ mm. The angle θ_t (in rad) is the azimuthal location, measured in a counterclockwise direction when viewed from above, of the insertion of the thermistor.

ID	$R - r$ (mm)	ξ	z (mm)	z/L	θ_t
V0-1	44.15	1.00	17.0	0.192	0
V0-2	44.15	1.00	22.1	0.250	0
V0-3	44.15	1.00	28.4	0.322	0
V0-4	44.15	1.00	39.1	0.443	0
V0-5	44.15	1.00	44.1	0.500	0
V0-6	44.15	1.00	50.5	0.572	0
V1-4	5.52	0.125	39.1	0.443	π
V1-5	5.52	0.125	44.1	0.500	π
V1-6	5.52	0.125	50.5	0.570	π
V0-7	44.15	1.00	66.2	0.750	π

We carried out heat-transport measurements (Sec. V A), the results of which largely agree with those of NG and thus show that the insertion of local temperature probes into the sample did not significantly alter this global property. Results for the LSF reported in Sec. V B indicate that the flow structure for LHC is more disorganized than it is for RBC and that this structure is significantly influenced by the vapor-bubble injection into the bulk. The results for the Reynolds numbers Re_U and Re_V corresponding to U and V are given in Sec. V C. Several other Reynolds numbers can be defined based on oscillation frequencies observed within the sample. The results for them are given in Secs. V D 1 and V D 2. The paper concludes with a discussion and summary of the most important results in Sec. VI.

II. CONTROL AND RESPONSE PARAMETERS

We studied convection in cylindrical cells of diameter D and height L. The horizontal bottom plate was heated to a temperature T_b and the parallel top plate was cooled to a temperature T_t. When $\Delta T = T_b - T_t$ is not too large, fluid properties can be assumed to be constant and the Oberbeck-Boussinesq approximation applies [39,40]. In that case the Rayleigh number

$$\mathrm{Ra} = \frac{\alpha g \Delta T L^3}{\nu \kappa} \tag{1}$$

and the Prandtl number

$$\mathrm{Pr} = \frac{\nu}{\kappa} \tag{2}$$

specify the state of the system. Here g is the gravitational acceleration and α, κ, and ν are the isobaric thermal expansion coefficient, the thermal diffusivity, and the kinematic viscosity at the center temperature. In addition, the aspect ratio

$$\Gamma \equiv D/L \tag{3}$$

specifies the geometry of the cylindrical sample. A global response of the system to the applied temperature difference is the heat flux from the bottom to the top plate as expressed by the Nusselt number

$$\mathrm{Nu} = \frac{QL}{A\lambda\Delta T}, \tag{4}$$

which relates the overall heat-current density Q/A to the purely conductive heat flux $\lambda\Delta T/L$ in the absence of convection (λ is the thermal conductivity of the fluid). As discussed in the Introduction, in our system only a central circular area A_h smaller than A was heated while the cooling area at the top plate A_c was equal to A. In Eq. (4) we used A_h, as was done also by NG [29].

Another system response is a turbulent flow with a vertical velocity component $u(t)$ that has a mean value

$$U = \langle u(t) \rangle \tag{5}$$

($\langle \cdots \rangle$ denotes the time average). This mean velocity will vary with the location within the sample. In RBC where the LSC corresponds to a single convection roll it vanishes at the sample center and its absolute value reaches a maximum near (but not too near) the sidewall (see, for instance, Ref. [8]). It is described by the dimensionless Reynolds number

$$\mathrm{Re}_U = \frac{UL}{\nu}. \tag{6}$$

The local velocity, in addition to having a nonzero mean value almost everywhere, is also highly fluctuating. Thus other quantities of interest are the root-mean-square fluctuation velocity

$$V = \langle [u(t) - U]^2 \rangle^{1/2} \tag{7}$$

and the associated Reynolds number

$$\mathrm{Re}_V = \frac{VL}{\nu}. \tag{8}$$

In RBC V is much more uniform throughout the sample than is U.

Reynolds numbers also can be defined in terms of the periods or frequencies of several experimentally accessible signals. One of these is the period $\mathcal{T}^{ac}$ of oscillations in the temperature time series measured with thermistors imbedded in the sidewall. In addition, the period $\mathcal{T}^{sl}$ of a lateral displacement of the LSC circulation plane (the sloshing mode) can be deduced from a Fourier analysis of eight azimuthally distributed sidewall temperatures. Finally, an oscillation frequency f_0 can be determined from temperature time series determined locally within the fluid. These Reynolds numbers are give by

$$\mathrm{Re}_{ac} = \frac{L^2}{\nu \mathcal{T}^{ac}}, \quad \mathrm{Re}_{sl} = \frac{L^2}{\nu \mathcal{T}^{sl}}, \quad \mathrm{Re}_{f_0} = \frac{L^2 f_0}{\nu}. \tag{9}$$

It is found that Re_{sl}, Re_{ac}, and Re_{f_0} are equal to each other within experimental error. We will describe locations within the sample by the vertical distance z or z/L from the bottom plate and by the radial location

$$\xi \equiv 1 - r/R, \tag{10}$$

where r is the horizontal distance from the vertical centerline and $R = D/2$ is the sample radius.

III. EXPERIMENTAL PROCEDURE

A. Apparatus

The apparatus is shown schematically in Fig. 1 and was described before by NG [29]. The cylindrical cell in which the convection took place was located in a dry can and was surrounded by air. All empty spaces within the can were filled with foam to prevent convection of the air and to thus reduce radial heat flux out of the cell. The temperature of the sapphire top plate was held constant by a circulating-water bath of temperature T_t^*. The outflow of the circulating water surrounded the can, thus providing a constant-temperature environment. A copper cylinder with a diameter $D_h = 2.54$ cm was glued to the center of the silicon bottom plate and was heated to a temperature T_b^*. Because T_t^* and T_b^* are the temperatures of the plates at the outside of the cell, a small correction was made to obtain the temperatures of the bottom plate T_b and top plate T_t in contact with the fluid (see Ref. [29]).

The central heated area of the bottom plate coincided with an area of the silicon wafer covered by cylindrical cavities with a diameter of 30 μm and a depth of 100 μm, arranged on a triangular lattice. The center-to-center distance between two neighboring cavities was $l = 600$ μm, resulting in a total of $N = 1570$ cavities. Bubble formation at the cavities is illustrated in Fig. 2 by a snapshot taken from above.

We used two cells (A and B) described in detail below in Secs. III B and III C, respectively. They were of the same size and shape but had different arrangements of local temperature probes. They had a height $L = 88.3$ mm and an aspect ratio $\Gamma = 1.00$.

The applied temperature difference was nominally constant, but actually ranged from about 15.8 K to about 16.8 K. The bottom temperature was varied from about 29.9 °C to about 41.7 °C so as to cover a range of superheat values. The nominally constant Rayleigh number varied from about 1.7×10^{10} to about 2.0×10^{10}.

The mean-flow Reynolds number Re_U in RBC varies with position and thus comparison between various measurements is complicated. However, in the bulk of RBC the fluctuation Reynolds number Re_V depends only weakly on position and comparison with other work is more direct. Thus we mention here that Re_V was measured for RBC over a wide range of Pr and Ra by Lam *et al.* [41].

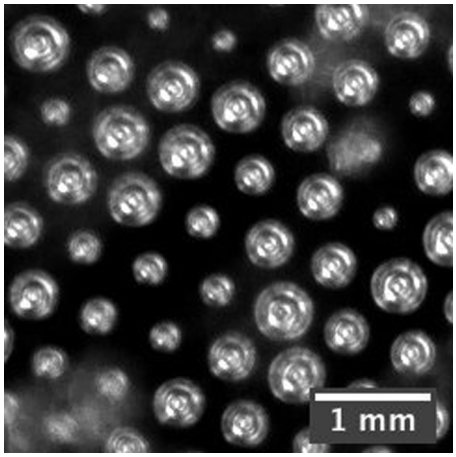

FIG. 2. Image of bubble formation at bottom-plate cavities as viewed from the top (from NG [29]). Bubbles form only at the cavities on a triangular lattice.

Their data could be represented by $\mathrm{Re}_V = 0.84\,\mathrm{Ra}^{0.40}\mathrm{Pr}^{-0.86}$. For our typical value $\mathrm{Ra} = 1.85 \times 10^{10}$ and our Pr close to 8 this yields $\mathrm{Re}_V \simeq 1800$.

B. Cell A

As described elsewhere (see, e.g., Ref. [13]), 24 thermistors were located in blind holes in the sidewall of cell A, with each of them yielding a local temperature measurement. Groups of eight were each equally spaced azimuthally at the three heights $z/L = 0.25$, 0.50, and 0.75. These vertical locations will be identified as $k = b$, m, and t, respectively. Relative to an arbitrarily chosen origin, the thermistors were located at azimuthal positions $\theta_{t,i} = (2i + 1)\pi/8$, $i = 0, \ldots, 7$, in the counterclockwise direction when viewed from above. The blind holes had a depth of 5.3 mm, which made the distance between the thermistors and the fluid as small as possible. This cell had no thermistors located in its interior.

The analysis for cell A was based on 24 simultaneous temperature time series obtained from the 24 thermistors for each set of external constraints (the superheat value and one- or two-phase flow). The time series consisted of typically 2×10^4 data points for each thermistor at time intervals of $\delta t \simeq 1.9$ s, thus covering a time span of more than 10 h.

C. Cell B

As for cell A, cell B had eight thermistors at the same azimuthal positions and in blind holes in the sidewall at the midheight $z/L = 0.50$ (but not at $z/L = 0.25$ and 0.75). In addition, there were ten Honeywell type-111-104HAK-H01 thermistors inside the fluid at the locations given in Table I. As shown in Fig. 3, they were mounted on ceramic rods with a diameter of 0.80 mm as

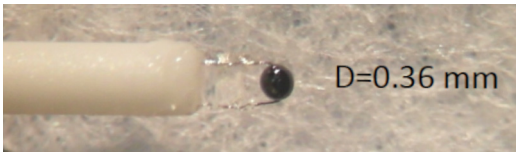

FIG. 3. Photograph of a type-111-104HAK-H01 (0.36-mm-diam) thermistor mounted through its 0.9-mm-diam ceramic rod. Adapted from Fig. 2 of Ref. [21].

TABLE II. Identifiers ID_1 and ID_2 of thermistor pairs used to evaluate the time intervals τ_p and τ_d. The spacings between the members of the pairs are δz and the mean vertical locations of the pairs are $\bar{z}/L$.

Set	ID_1	ID_2	ξ	δz (mm)	$\bar{z}/L$	θ_t
1	V0-1	V0-2	1.00	5.1	0.221	0
1	V0-2	V0-3	1.00	6.3	0.286	0
1	V0-1	V0-3	1.00	11.4	0.272	0
2	V0-4	V0-5	1.00	5.0	0.472	0
2	V0-5	V0-6	1.00	6.4	0.536	0
2	V0-4	V0-6	1.00	11.4	0.508	0
3	V1-4	V1-5	0.125	5.1	0.472	π
3	V1-5	V1-6	0.125	6.4	0.536	π
3	V1-4	V1-6	0.125	11.4	0.508	π

described in Refs. [21,22,42]. We did not observe measurable effects of bubble-probe interactions. The rods were inserted through holes, also of nominally 0.80 mm diameter, in the 6.4-mm-thick plexiglass sidewall. While the vertical hole locations in the wall were known with high accuracy, there were two possible contributions to the uncertainties of the vertical thermistor locations. One came from any tilt of the rods relative to a line orthogonal to the cylinder axis. We believe this to be very small, probably no more than 0.2 mm on the sample axis ($\xi = 1.00$) and much less near the sidewall ($\xi = 0.125$). Another possible contribution came from the suspension of the thermistors by their 0.10-mm-diam platinum leads (see Fig. 3). Because of the fragile nature of these leads, the vertical position of the thermistor center is estimated to be uncertain by about 0.3 mm. Thus the total uncertainty is close to 0.5 mm. Similarly, we estimate that the uncertainty of the distance δz between adjacent thermistors is about 0.7 mm. This number will be used below for the error bars in Fig. 7.

As indicated in Table II, there were three sets, each consisting of three thermistors. For each set there was a vertical distance of about 5.1 mm between the lower and middle thermistors and about 6.3 mm between the middle and upper thermistors. Thus three cross-correlation functions could be obtained from each set, as indicated in Table II. The middle thermistor of the two sets on the vertical centerline (i.e., $\xi = 1.00$) was located at $z/L = 0.25$ and 0.50. The third set was located near the sidewall at $\xi = 0.125$, with its middle thermistor at $z/L = 0.50$. Finally, a single thermistor was located on the centerline ($\xi = 1.00$) at $z/L = 0.75$.

For cell B the time interval of consecutive temperature measurements was $\delta t = 0.06$ s. In that case a single data segment could gather 50 000 data points per thermistor, corresponding to about 50 min. At each superheat 20 such segments were measured and correlation functions and spectra were calculated from each segment and averaged over all 20.

D. Working fluid and bubble nucleation

The working fluid was Novec™-7000 manufactured by 3M™. Its physical properties are well documented [43]. It was chosen because it has the experimentally convenient relatively low boiling temperature $T_\phi \simeq 34\,^\circ$C at atmospheric pressure. The fluid in the cell was connected to a reservoir placed at an elevation of 1.16 m above the bottom plate. The surface of the fluid in the reservoir was exposed to atmospheric pressure and at the bottom plate provided a hydrostatic pressure of 16.0 ± 0.3 kPa in addition to atmospheric pressure. The properties needed to evaluate Ra, Pr, Nu, and Re were evaluated at the measured center temperature T_c (for details see [29]). The Prandtl number was close to eight for all measurements.

The filling procedure of the cell and the measurement protocol were described in detail by NG [29]. During all of our measurements the bubbles emanating from the bottom plate redissolved before reaching the top plate; thus no vapor layer ever formed above the liquid. Our goal was to

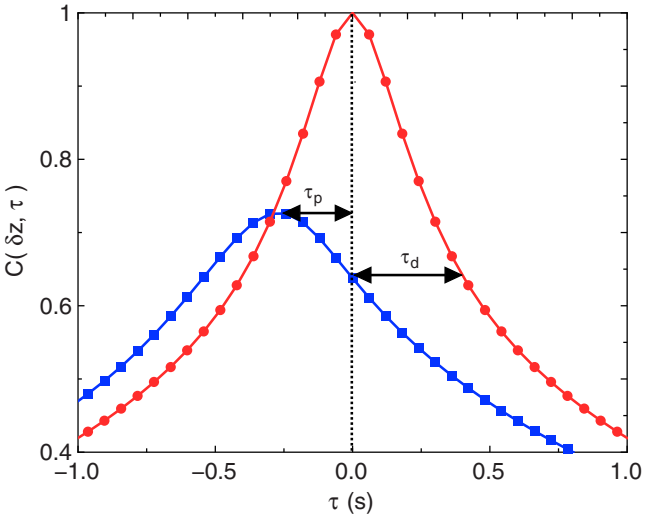

FIG. 4. Autocorrelation function (red circles) and cross-correlation function (blue squares) for $T_b - T_{on} = 10.6$ K and two-phase flow of thermistors V1-5 and V1-6 ($\delta z = 6.4$ mm; see Tables I and II). The autocorrelation function is the average of those at the two locations. The time intervals $\tau_p = -0.266$ s and $\tau_d = 0.407$ s are illustrated by the arrows.

better understand the flow profile in one-phase flow as well as in two-phase flow and to measure the corresponding Reynolds numbers for different values of superheat, while keeping the thermal forcing ΔT constant.

The data presented in the paper are all well converged. However, unavoidably there are also systematic errors. For those connected with the sample-filling process, etc., the scatter of the data provides an estimate on the error of the measurements.

IV. PREDICTIONS AND TESTS OF THE ELLIPTIC APPROXIMATION

A. Range of applicability of the elliptic approximation

The EA [31] is a second-order Taylor-series expansion of the correlation function $C(\tau,\delta z)$ in space and time about $C(0,0) = 1$. Thus it is a controlled approximation valid for sufficiently small time and space increments τ and δz. It shows that, for small τ and δz, contours of equal correlation in the τ-δz plane are ellipses. In the derivation of local velocities from temperature correlation functions it is assumed that temperature behaves as a passive scalar; this is the case in the bulk of RBC as shown in Refs. [33,34]. The EA is valid in turbulent systems with strong fluctuations, such as RBC, where the Taylor frozen-flow approximation (see, e.g., [44]) is not applicable.

As can be seen from Figs. 4 and 6, the maximum values of the cross-correlation functions are well below unity. Thus one might expect that the EA would fail for data such as those in these figures. However, He and co-workers [31,36] argued that the applicability of the EA extends to exceptionally large values of τ and δz because of the Kolmogorov similarity hypothesis, which implies that, in the inertial range of δz and τ, the contours of equal correlation should remain elliptic with the same axis ratio and orientation as those found by the EA. The relevant predictions of the EA are determined entirely by the axis ratio and orientation; thus these predictions should be applicable over the entire inertial range even though the value of the correlation function on a given contour is well below unity and for that reason may differ significantly from that predicted by the EA. Their analysis [36] of channel-flow data from numerical simulation supported their argument. There they found that even data with a maximum value of $C(\tau,\delta z)$ as small as about 0.4 conformed to the predictions of

the EA. We will refer to the extension of the EA predictions to this extended range of space and time as the elliptic model (EM).

B. Predictions of the elliptic approximation

Detailed derivations and summaries of relevant EA predictions were given in Ref. [42] and the Supplemental Material of Ref. [45]. Here we summarize the results needed to evaluate the present measurements.

It follows from the EA that $C(\delta z,\tau)$ can be written as a function of a single variable z_E:

$$C(\delta z,\tau) = C(z_E,0). \tag{11}$$

Here z_E is the rescaled length

$$z_E = \sqrt{(\delta z - U\tau)^2 + (V\tau)^2}, \tag{12}$$

where U is a component of the mean-flow velocity (5) and V is the root-mean-square deviation from U [Eq. (7)]. Further predictions of the EA are given in terms of two time intervals τ_p and τ_d that are obtained from the autocorrelation functions at two points in space (which, for a homogeneous system, are equal to each other) and the corresponding cross-correlation function. Figure 4 shows an example. As illustrated, τ_p is the location along the time-delay axis of the maximum of the cross-correlation function, while τ_d is the time at which the autocorrelation functions have decayed to the same value as that of the cross-correlation function at $\tau = 0$.

For δz small enough for the EA predictions to be applicable τ_p and τ_d are proportional to δz:

$$\tau_d = \alpha_0 \delta z, \quad \tau_p = \alpha_p \delta z. \tag{13}$$

In terms of α_p and α_0 the EA predicts that

$$V_{\text{eff}} \equiv \sqrt{U^2 + V^2} = 1/\alpha_0, \tag{14}$$

$$U = \alpha_p/\alpha_0^2, \tag{15}$$

and

$$V = \frac{\sqrt{1 - (\alpha_p/\alpha_0)^2}}{\alpha_0}. \tag{16}$$

We used Eqs. (15) and (16) to determine U and V. The results for U and V and Eq. (12) were used to compute z_E.

Based on the EA, one can derive a space-time equivalence that makes it possible to obtain the spatial temperature spectrum $E(k)$ from the temporal temperature spectrum $P(f)$. The equivalence is obtained by transforming the time coordinate to the spatial coordinate according to

$$z = V_{\text{eff}}\tau, \tag{17}$$

where V_{eff} is given by Eq. (14).

C. Expected range of applicability of the EM for the experimental conditions of this study

We show in Fig. 5 the normalized power spectrum of the temperature measured at the sample center (other locations yield consistent results but are less definitive because of the appearance of a peaks in the spectrum from the sloshing and/or torsional modes in the lower decade of the inertial range). One sees that there is no wide range of the frequency over which a unique power law gives a good fit. This is due primarily to the onset of viscous dissipation already at frequencies somewhat below 1 Hz. However, as indicated by the solid line, there is a range over which the Obukhov-Corrsin spectrum [46,47] with an exponent of $-5/3$ fits the data. Deviations from this power law at low frequencies occur below about 0.4 Hz and this frequency might be used as an estimate of the lower

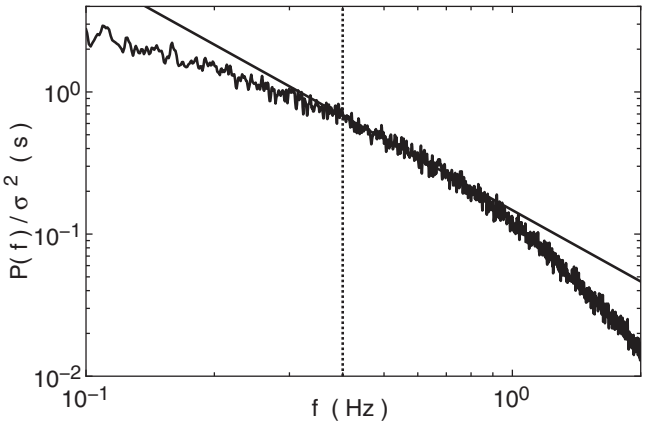

FIG. 5. Normalized temperature power spectrum $P(f)/\sigma^2$ as a function of the frequency f in Hz for $T_b - T_{on} = 10.6$ K and two-phase flow at the sample center. The solid line is a power-law fit with the exponent fixed at $-5/3$. The vertical dotted line indicates an estimate of the lower limit of an inertial range at about 0.4 Hz.

limit f_I of the inertial range. A similar analysis, but using an exponent of $-7/5$ as suggested by Bolgiano [48] and Obukhov [49], yields a similar, albeit slightly lower, value of about 0.3 Hz. Similar results are obtained for all of our runs. Thus we estimate that in our experiment the inertial range covers time intervals smaller than $1/f_I = \tau_I \simeq 2.5$ s.

For the example of Fig. 5 the EA analysis yielded $V_{\rm eff} = 9.5$ mm/s (for all of our runs we found $V_{\rm eff} \gtrsim 6$ mm/s), thus indicating [Eq. (17)] that the inertial range in this case would extend up to about $\delta z_I = \tau_I V_{\rm eff} \simeq 24$ mm. If the arguments of He and Yang regarding the range of applicability of the EA are valid, then we would expect that our values of $\delta z \lesssim 12$ mm and our results for $|\tau_p| \lesssim 0.9$ s and $\tau_d \lesssim 1.8$ s are small enough.

D. Tests of the applicability of the elliptic approximation to our measurements

Several previous experiments used the EA predictions to derive velocities from correlation-function measurements [37,38,42,50,51]. Some of these have demonstrated the applicability of the EA predictions to time and space increments τ and δz well beyond those expected for a second-order expansion of $C(\tau,\delta z)$. Here we examine the applicability of the EA predictions to our measurements.

1. Correlation functions and homogeneity

One of the assumptions of the EA is that the sample is homogeneous over the distances between the probes used in the measurements. Thus, one obvious requirement is that the two autocorrelation functions used to determine τ_d (see Fig. 4) should coincide. In real experiments the homogeneity assumption will generally not be satisfied exactly and the issue then becomes whether deviations from it are sufficiently small for the EA to yield useful results for U and V.

In Fig. 6 we show examples for two locations in our sample (see Table II) of autocorrelation functions $C(\tau,0)$ and cross-correlation functions $C(\tau,\delta z)$ for two-phase flow with a superheat of 7.82 K. Results at the third location for other superheat values and for one-phase flow are similar. From the autocorrelation functions one sees that there are significant deviations from homogeneity. It is difficult to estimate the errors introduced by this. In the determination of τ_d (see Fig. 4) we used the average of the two autocorrelation functions that corresponded to the cross-correlation function under consideration. The average of the two values of τ_d obtained by using the two autocorrelation functions separately had essentially the same value. This procedure cannot be expected to completely cancel errors due to spatial inhomogeneity because this inhomogeneity introduces odd terms into

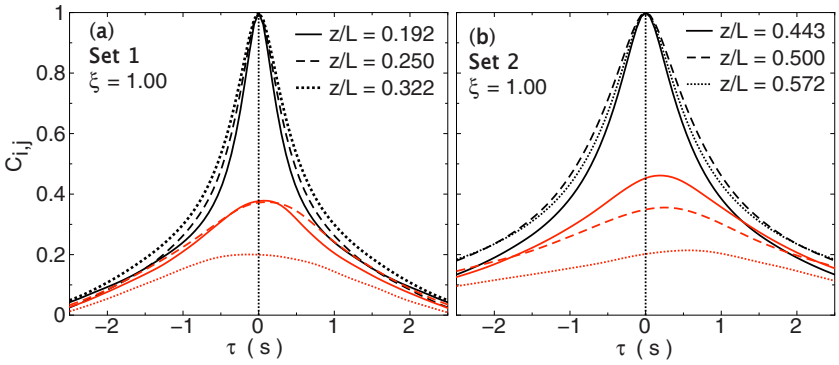

FIG. 6. Examples of correlation functions. In each set the upper three curves are the autocorrelation functions at the locations z/L and ξ given in the figure (see also Table I). The lower three curves (red) are the three corresponding cross-correlation functions for (a) (see Table II) $\bar{z}/L = 0.221$ and $\delta z = 5.1$ mm (solid line), $\bar{z}/L = 0.286$ and $\delta z = 6.3$ mm (dashed line), and $\bar{z}/L = 0.272$ and $\delta z = 11.4$ mm (dotted line) and (b) $\bar{z}/L = 0.472$ and $\delta z = 5.0$ mm (solid line), $\bar{z}/L = 0.536$ and $\delta z = 6.4$ mm (dashed line), and $\bar{z}/L = 0.508$ and $\delta z = 11.4$ mm (dotted line). All results are for two-phase flow and $T_b - T_{on} = 7.82$ K.

the Taylor-series expansion of $C(\tau,\delta z)$ and the effect of these terms is difficult to estimate. We do not think that these errors are very large because the overall analysis gave consistent results over the entire range of $T_b - T_{on}$, of δz (see Fig. 7), and for two-phase and one-phase flow (see Sec. V C below).

2. *Dependence of τ_p and τ_d upon δz*

An important test of the applicability of the EM is the dependence of τ_p and τ_d upon the displacement δz; these time intervals should be proportional to δz [Eq. (13)]. Representative results are shown in Fig. 7. The horizontal error bars correspond to the uncertainty of δz, which are evaluated from the estimated absolute error of δz that is approximately 0.7 mm (see Sec. III C). Contributions from measurement errors to the uncertainties of the time intervals are negligibly small (less than 0.01 s); however, systematic errors due to the spatial inhomogeneities discussed above may be significant but are difficult to estimate. The data are generally consistent with the expected proportionality to δz, thus supporting the applicability of the EA results to relatively large time and space intervals that are, however, well within the inertial range indicated by the temperature spectra (see Fig. 5).

It is interesting to note that the deviations from the fitted straight lines in Figs. 7(c) and 7(d) are very similar. These measurements correspond to the same spatial locations, but Fig. 7(c) is for two-phase flow and Fig. 7(d) is for one-phase flow. This suggests that the errors are due primarily to errors of δz and only to a lesser extent to errors of τ_p and τ_d.

3. *Dependence of the correlation functions upon z_E*

Another test of the EA is based on a central result of the EA, which shows that $C(\delta z,\tau)$ can be written as a function of a single variable z_E. Having determined U and V from Eqs. (13)–(16) and data such as those in Fig. 7, we can obtain z_E as a function of τ and δz from Eq. (12). Figure 8 shows results corresponding to the correlation functions in Fig. 6. The deviations from homogeneity are shown in the plots of the autocorrelation functions (closed symbols). However, the results for the three cross-correlation functions fall within the range of the autocorrelation functions and suggest that deviations from a unique curve for all functions are likely to be caused by the small inhomogeneity of the sample over the measurement distance rather than a failure of the EA.

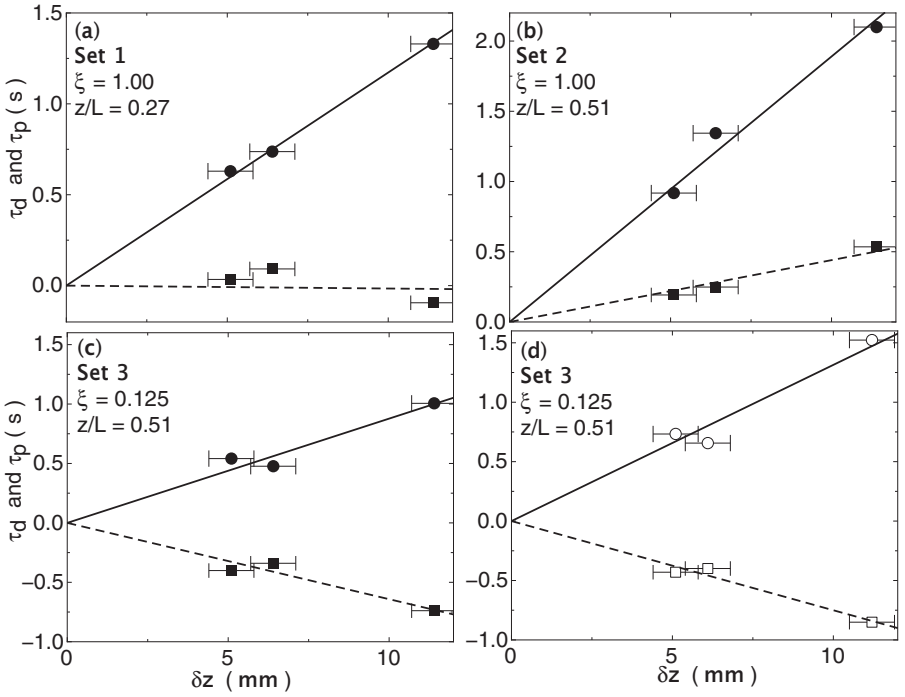

FIG. 7. Plots of τ_p (squares) and τ_d (circles) as a function of δz for (a)–(c) two-phase flow and $T_b - T_{on} = 7.82$ K (run 1 511 203) and (d) one-phase flow and $T_b - T_{on} = 8.45$ K (run 1 512 075). The data yield (a) $\alpha_p = -0.002$ and $\alpha_0 = 0.117$ s/mm, (b) $\alpha_p = 0.044$ and $\alpha_0 = 0.189$ s/mm, (c) $\alpha_p = -0.064$ and $\alpha_0 = 0.088$ s/mm, and (d) $\alpha_p = -0.075$ and $\alpha_0 = 0.131$ s/mm.

V. RESULTS

A. Heat transport

The only differences between the two samples A and B, on the one hand, and those of NG [29], on the other, were the numbers and locations of thermistors. To check whether these differences impacted the heat transport, Nusselt numbers were measured for both cells in the one-phase and

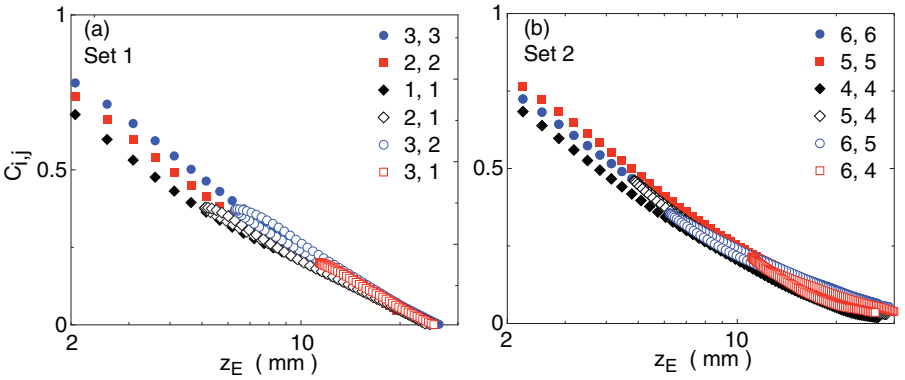

FIG. 8. Examples of plots of correlation functions $C_{i,j}(\tau,\delta z)$ as a function of z_E [Eq. (12)]. The values of i and j are given in the figure. All data are for two-phase flow and $T_b - T_{on} = 7.82$ K.

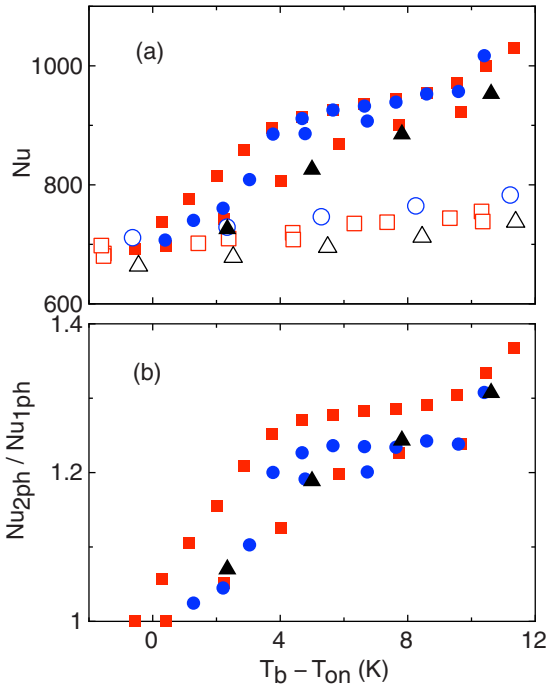

FIG. 9. (a) Nusselt number for one-phase flow Nu_{1ph} (open symbols) and two-phase flow Nu_{2ph} (closed symbols) and (b) the ratio Nu_{2ph}/Nu_{1ph} as a function of the superheat $T_b - T_{on}$. Blue circles show cell A, black triangles cell B, and red squares the results of NG [29].

two-phase flows. The results are compared with those of NG in Fig. 9. For both cells they fall within the spread between the different data sets of the earlier work.

B. Large-scale flow

1. *Qualitative nature of large-scale flow*

Shadowgraph flow visualizations by NG [30] indicated that, in the presence of bubbles (two-phase flow), there was a LSF at least in the lower portion of the sample. It carried hot plumes, emitted mostly by the thermal boundary layer just above the central heated part of the bottom plate, to one side where the plumes then rose near the sidewall toward the top plate. This is illustrated in Fig. 10(a) and more clearly by Movie 3 of Ref. [30]. Cold plumes generated similarly under the entire top plate tended to move toward the other side of the cell where they descended; however, their signature became weaker as the bottom plate was approached and it is not clear whether the plume motion was indicative of a closed-loop LSC in the form of a single convection roll.

In the absence of bubbles (one-phase flow) hot plumes were rising more or less vertically from the bottom plate and their motion did not reveal any evidence of a LSF. Cold plumes did suggest some lateral LSF just under the top plate, but their descent through the bulk did not reveal any evidence for a closed LSC roll. This is shown in Fig. 10(b) and more clearly in Movie 4 of Ref. [30].

2. *Quantitative measurements of large-scale flow*

We searched for a LSF using the thermistors immersed in the sidewall. Each set of eight thermistors, azimuthally distributed uniformly around the circumference, yielded temperatures $T_{k,i}$,

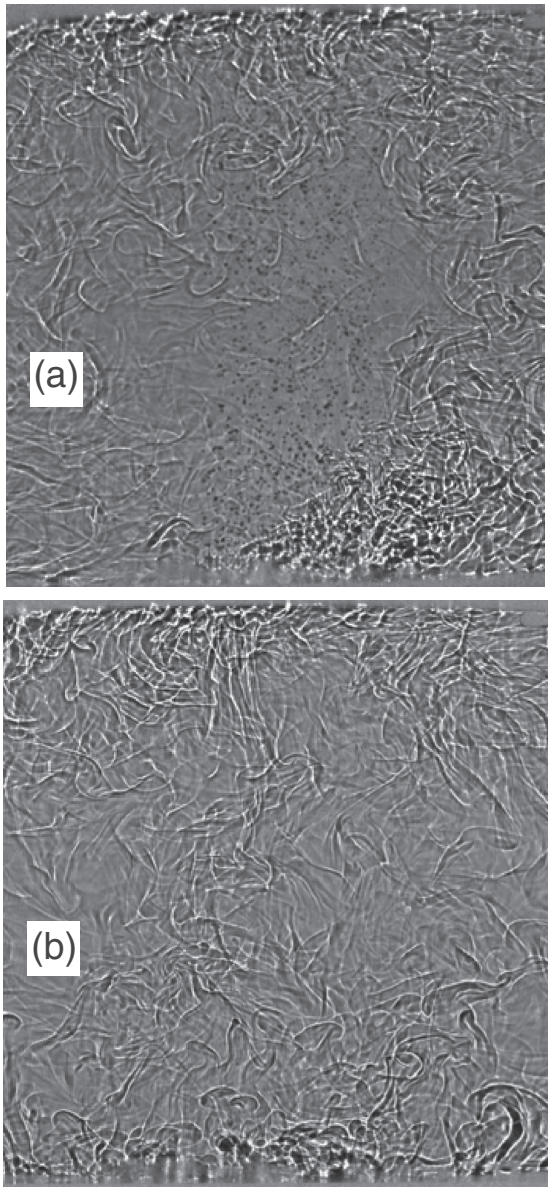

FIG. 10. Shadowgraph images taken from the side for (a) two-phase and (b) one-phase flow (from NG [30]). They show a horizontal average over the entire width of the sample. The tiny dark dots in (a) (hardly visible) rising through the center are the bubbles. The corresponding movies in the Supplemental Material of Ref. [30] reveal a more detailed picture of the flow dynamics.

$i = 0,1,2,\ldots,7$, at a given measurement time. The function

$$T_f = T_{0,k} + \delta_k \cos[i\pi/4 - \theta_{0,k}] \tag{18}$$

was fit to them, separately at each height $k = b,m,t$ and at each measurement time. The least-squares adjusted parameters $T_{0,k}$, δ_k, and $\theta_{0,k}$ describe an azimuthally uniform background temperature, a temperature amplitude of the LSF, and the azimuthal orientation of a large-scale upflow, respectively (see, e.g., Refs. [11,13] for more details).

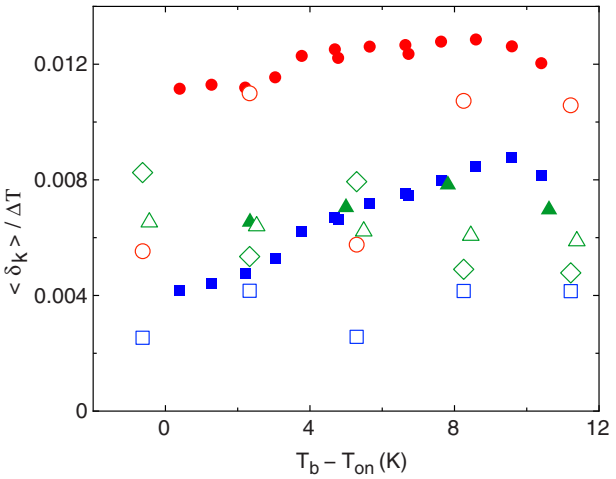

FIG. 11. Scaled temperature amplitude $\langle\delta_k\rangle/\Delta T$ of the LSF. Red circles, green diamonds, and blue squares correspond to the lower ($k = b$), middle ($k = m$), and upper ($k = t$) sets of thermistors in cell A, respectively. The green triangles are for $k = m$ of cell B. Open symbols show one-phase flow and closed symbols two-phase flow.

Results for $\langle\delta_k\rangle/\Delta T$ are shown in Fig. 11 as a function of the superheat. One can see that any coherent structure leading to an azimuthal cosine variation, if present at all, is strongest near the bottom of the sample ($k = b$, red circles). However, at the Rayleigh numbers $\mathrm{Ra} \simeq 2 \times 10^{10}$ of the experiment, measurements for (uniformly heated) RBC at the same Pr and $\Gamma = 1.00$ [52] give $\langle\delta_k\rangle/\Delta T \simeq 0.017$, which is significantly larger than the data in Fig. 11 for LHC. The indication of an azimuthally varying structure for $k = b$ ($z/L = 0.25$ $\langle\delta_b\rangle/\Delta T$) is consistent with the visualization shown in Fig. 10(a) for two-phase flow, but Fig. 10(b) for one-phase flow in general gives no indication of a LSF. Indeed, we see from the results for $\langle\delta_b\rangle/\Delta T$ and one-phase flow (red open circles) that $\langle\delta_b\rangle/\Delta T$ values near those for two-phase flow (red closed circles) are reached only in some of the runs and not, for instance, for superheats of -0.6 and 5.3 K. Inspection of the time series for one-phase flow and superheats of -0.6 and 5.3 K suggests that the data are statistically reliable (i.e., not seriously affected by inadequately long averaging times). We believe that they are suggestive of multistability, but a more detailed investigation of this issue would be desirable. The overall indication of a poorly defined LSF, especially for single-phase flow, is consistent with the flow visualization illustrated in Fig. 10 and the corresponding movies in the Supplemental Material of Ref. [30].

A useful additional indicator of the LSF strength is based on a Fourier decomposition of the $T_{k,i}$ at a given k [53–55]. This yields the Fourier coefficients $A_{k,j}$ (the cosine coefficients) and $B_{k,j}$ (the sine coefficients) where $j = 1, \ldots, 4$ identifies the $N = 4$ Fourier modes accessible with eight temperatures. The energy

$$E_{k,j}(t) = A_{k,j}^2(t) + B_{k,j}^2(t) \tag{19}$$

for each mode and the sum $E_{k,\mathrm{tot}}(t)$ of the four energies were calculated. The parameter

$$S_k = \max\left[\frac{(N\langle E_{k,1}\rangle/\langle E_{k,\mathrm{tot}}\rangle - 1)}{(N-1)}, 0\right] \tag{20}$$

was proposed by Stevens *et al.* [54] as a useful indicator of the LSF strength and coherence. A value of S_k close to unity corresponds to a LSF where the cosine wave is well defined and dominates over fluctuations. Smaller values of S_k suggest a strongly fluctuating LSF structure and it was suggested in Ref. [54] that $S_k \lesssim 0.5$ is indicative of no dominant coherent structure with a characteristic length scale close to the sample height.

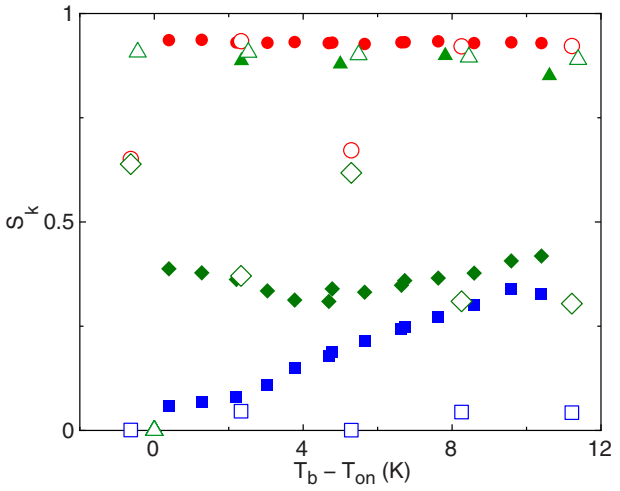

FIG. 12. Parameter S_k [Eq. (20)] describing the strength of the LSF. Red circles, green diamonds, and blue squares correspond to the lower ($k = b$), middle ($k = m$), and upper ($k = t$) sets of thermistors in cell A, respectively. The green triangles are for $k = m$ of cell B. Open symbols show one-phase flow and closed symbols two-phase flow.

Results for S_k are shown in Fig. 12 as a function of the superheat $T_b - T_{on}$. As in Fig. 11, the open (closed) symbols are for one-phase (two-phase) flow. One can see that for cell A only the lower part of the sample ($k = b$, red circles) yielded values of S_m close to one, as expected for a coherent structure extending over the diameter of the sample, and then reliably only for two-phase flow (red closed circles). Consistent with the $\langle\delta_b\rangle/\Delta T$ results (Fig. 11), the one-phase data yielded S_m close to one only for some of the runs. At higher levels in cell A ($k = m$ and t) the measurements provided no support for a coherent structure. One concludes that there is no coherent convection roll as is found in RBC (which leads to $S_k \simeq 1$ at all levels; see, e.g., [52]) and only upflow at a particular azimuthal orientation and near the sample bottom, which dissipates at larger heights.

The results for S_m of cell B (green triangles in Fig. 12) differ significantly from those of cell A (measurements for $k = b$ and t were not made in B; see Sec. III C). Even at the midplane ($k = m, z/L = 0.50$) the azimuthal structure is well defined for both one-phase and two-phase flow, with S_m close to one. This surprising result suggests that the formation of a coherent structure in cell B is *enhanced* by the obstructions due to the thermistors that were inserted into the sample (cell A had no internal thermistors), while one might have expected the opposite. We note, however, that the amplitudes $\langle\delta_m\rangle/\Delta T$ for cell B (Fig. 11, green triangles) are smaller than those for cell A and of similar size to $\langle\delta_m\rangle/\Delta T$ for cell A where the results for S_m (Fig. 12) indicate the absence of a well defined structure. Compared to RBC for the same Ra and Γ [52], we see that $\langle\delta_m\rangle/\Delta T$ for cell B is smaller by a factor of nearly 3.

C. Reynolds numbers based on the elliptic model

1. General remarks and results

We used the EM of He and co-workers [31,36] to determine the mean-flow velocity U [Eq. (5)] and root-mean-square fluctuation velocity V [Eq. (7)] from simultaneous temperature time series taken at several internal locations of cell B at time intervals of 0.06 s (see Sec. III C). The relationships derived from the EM that are relevant to our analysis were summarized in Sec. IV A. In Sec. IV C we discussed the ranges of time and space displacements τ and δz over which we expect the EM to be applicable based on the assumption of Kolmogorov self-similarity. In Sec. IV D we presented

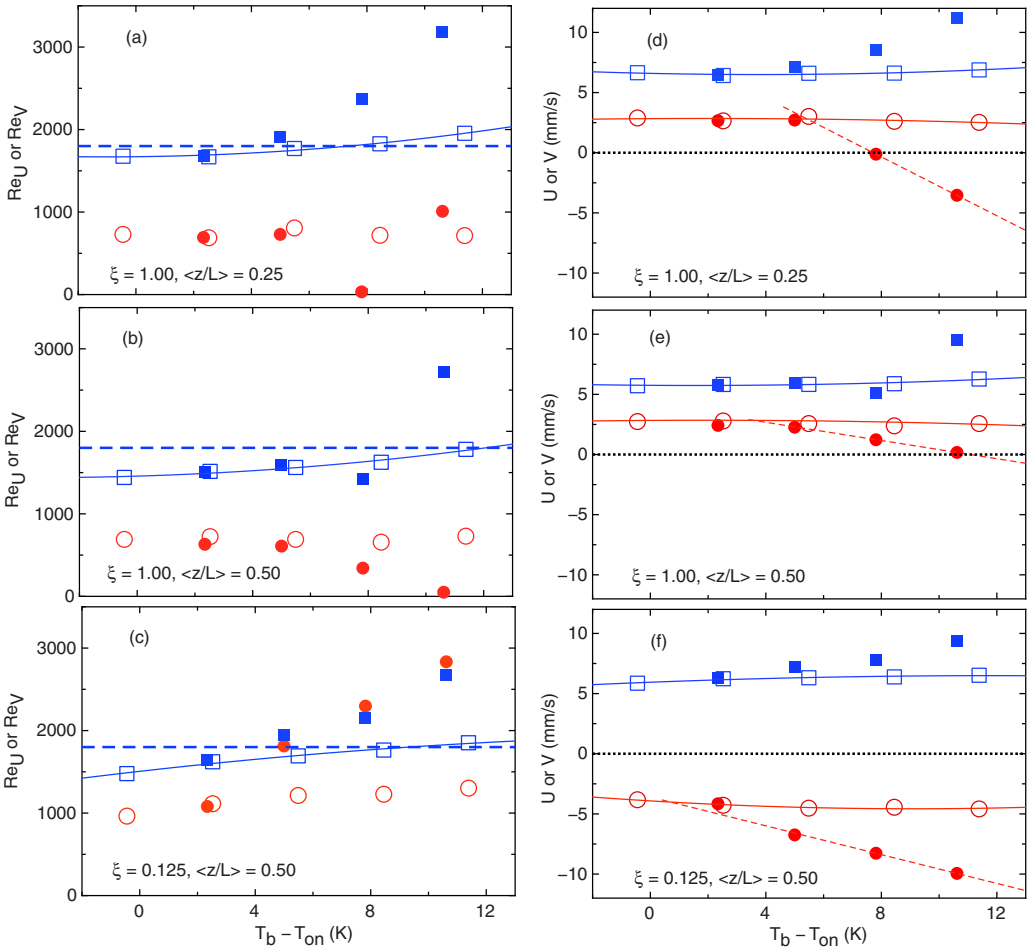

FIG. 13. (a)–(c) Reynolds numbers Re_U (red circles) and Re_V (blue squares) as a function of the superheat $T_b - T_{on}$. (d)–(f) Mean-flow velocity U (red circles) and root-mean-square fluctuation velocity V (blue squares) as a function of the superheat $T_b - T_{on}$. Open symbols show one-phase flow and closed symbols two-phase flow. Blue horizontal dashed lines show Re_V for RBC, solid lines show fits of a quadratic equation to the data, and red short-dashed lines show fits of a straight line to the two points with the largest $T_b - T_{on}$.

several tests of the applicability of the EM under the conditions of our experiment. These tests do not reveal any major problems with using the EM to analyze our data.

The measurement locations were at the same radial position and separated vertically by distances δz (see Table I). The velocity determinations required obtaining two time intervals τ_p and τ_d from measurements at pairs of nearby locations (see Fig. 4); these pairs and their δz values are listed in Table II. Each velocity determination was based on three sets of τ_p, τ_d, and δz, with each set derived from measurements at three vertical positions as indicated in Table II and described in Sec. IV A. The sets are associated with averaged locations $\bar{z}/L$ and ξ equal to 0.25 and 1.00 for set 1, 0.50, and 1.00 for set 2 and 0.50 and 0.125 for set 3 (the precise and detailed locations follow from Table II). The measurements thus are of the time-averaged vertical velocity and velocity-fluctuation components $U(\bar{z}/L,\xi)$ and $V(\bar{z}/L,\xi)$ [Eq. (7)]. The velocities were converted to Reynolds numbers Re_U [Eq. (6)] and Re_V [Eq. (8)] using the kinematic viscosity ν at the measured center temperatures T_c.

Results for Re_U, U, Re_V, and V are shown in Fig. 13. The red circles are for Re_U and U, while the squares give the results for Re_V and V. The top pair in Figs. 13(a) and 13(d), the middle pair in

Figs. 13(b) and 13(e), and the bottom pair in Figs. 13(c) and 13(f) are for sets 1, 2, and 3, respectively. Figures 13(a)–13(c) give the Reynolds numbers, while Figs. 13(d)–13(f) show the corresponding velocities in mm/s. It is helpful to show the velocities as well as the Reynolds numbers because U can be negative [see Fig. 13(f)] or even pass through zero as $T_b - T_{on}$ changes [see Fig. 13(d)] while $\mathrm{Re}_U \geqslant 0$. In order to facilitate the comparison between one-phase flow (open symbols) and two-phase flow (closed symbols), we fitted a quadratic polynomial to the one-phase data and show the fits as solid lines in the figure.

2. *One-phase flow*

Let us first consider the case of one-phase flow (open symbols). As expected, neither Re_U (open circles) nor Re_V (open squares) shows a significant dependence on the superheat because Ra does not change significantly (see Sec. III A). Comparison of Re_U with other measurements for RBC is not easy because Re_U depends strongly on the position in the sample. For RBC it is largest in the bulk near the sidewall, while it vanishes at the sample center. For our case of local heating with cooling over the entire top plate, we find that $\mathrm{Re}_U \simeq 800$ [Fig. 13(b)] and that there is upflow [$U \simeq 2.5$ mm/s > 0, Fig. 13(e)] at the sample center. This is consistent with the movie of Ref. [30] and Fig. 10(b), which show more or less vertically rising plumes distributed broadly in the horizontal direction rather than a closed single-cell LSC. Consistent with this flow, the data closer to the bottom plate and on the sample centerline for Re_U and U do not change much, as indicated by the results for set 1 shown in Figs. 13(a) and 13(d).

Closer to the sidewall the one-phase results for set 3 [$\xi = 0.125$, Figs. 13(c) and 13(f)] indicate a significant downflow ($U \simeq -4$ mm/s < 0). This is not unexpected because there must be downflow at least at some azimuthal locations when there is upflow through the central part of the sample.

As is the case for RBC, the results for the fluctuation velocity V and Re_V in one-phase flow do not depend very much on the location within the sample. Averaged over all measured superheats, one has $V = 6.63$ mm/s and $\mathrm{Re}_V = 1780$ for set 1 ($\xi = 1.00$ and $\bar{z}/L = 0.25$), $V = 5.90$ mm/s and $\mathrm{Re}_V = 1585$ for set 2 (sample center, $\xi = 1.00$ and $\bar{z}/L = 0.50$), and $V = 6.26$ mm/s and $\mathrm{Re}_V = 1682$ for set 3 (near the sidewall, $\xi = 0.125$ and $\bar{z}/L = 0.25$). These results are quite close to the result $\mathrm{Re}_V \simeq 1800$ estimated for RBC at the same Ra and Pr (see Sec. III A) and shown in Figs. 13(a)–13(c) by the horizontal dashed lines (blue).

3. *Two-phase flow*

For two-phase flow the data in Fig. 13 reveal a number of remarkable features. We note that the rising bubbles (closed symbols) at sufficiently large superheat modify not only the mean-flow velocity U and Re_U, but also the fluctuation velocity V and Re_V. Further, the influence of the bubbles does not begin as soon as they are formed when $T_b - T_{on}$ exceeds zero; rather, there is a finite onset value δT_{2ph} of $T_b - T_{on}$ below which the rising bubbles have no influence at the measurement positions of the present work. This is most clearly seen from the results for U in Figs. 13(d)–13(f). The results for the onset of enhancement of V are not as clear, but within our resolution the onset is the same as it is for U. There seems to be an exception or complication for set 2 [Figs. 13(b) and 13(e)] where the result for V at a superheat of 7.9 K is lower in the two-phase system than it is for the corresponding one-phase flow even though based on all other data we would have expected an enhancement. We have no explanation for this outlier. The onset shift is largest (with δT_{2ph} a little over 5 K) along the centerline in the lower part of the sample. At the sample center we find $\delta T_{2ph} \simeq 4$ K, while near the sidewall δT_{2ph} seems to be close to zero.

For $T_b - T_{on} > \delta T_{2ph}$, the amplitude of U is *reduced* by the bubbles of two-phase flow for sets 1 and 2 and along the centerline (where it was positive for one-phase flow) even changes sign, whereas the amplitude of U in set 3 increases with superheat. It is not possible to say whether this effect is due directly to bubble influence or indirectly to changes in the large-scale flow structure induced by the bubbles.

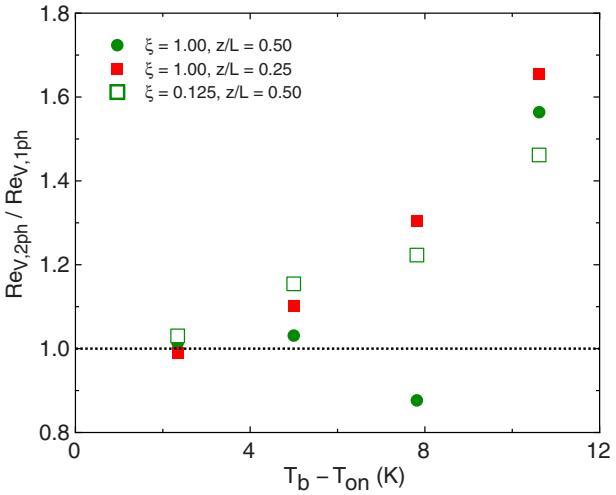

FIG. 14. Ratio $\mathrm{Re}_{V,2ph}/\mathrm{Re}_{V,1ph}$ as a function of the superheat $T_b - T_{on}$.

The fluctuation velocity V (as well as Re_V), on the other hand, is *enhanced* by the bubbles of the two-phase flow [except for the anomaly mentioned above and seen in Figs. 13(b) and 13(e)]. This effect is consistent with direct numerical simulations with bubble injection [56–59], which also found that velocity fluctuations were enhanced in two-phase flow, with the enhancement increasing with increasing rate of bubble injection. Note that in these simulations the vapor-bubble nucleation process is not modeled. Instead, a certain and controlled number of nuclei is imposed. These then grow or shrink, depending on the local conditions. The experimentally observed enhancement of velocity fluctuations stands in contrast to the *reduction* of temperature fluctuations found by Narezo Guzman *et al.* [29]. The diminished temperature fluctuations may be attributed to a smoothing of the temperature field due to the enhanced mixing by the larger velocity fluctuations. This reduction of the temperature fluctuations by the bubbles was found also in numerical simulations [59], where the temperature field became much less intermittent in the presence of the vapor bubbles due to the smoothing of sharp temperature fronts.

In Fig. 14 we provide a more quantitative comparison of Re_V in one-phase and two-phase flow by showing the ratio $\mathrm{Re}_{V,2ph}/\mathrm{Re}_{V,1ph}$ as a function of the superheat. At the larger superheats one can see that the relative fluctuation enhancement is similar at all three locations in the sample and reaches values as large as 60% or so.

D. Reynolds numbers from frequency measurements

It has long been known from single-point determinations in RBC samples of the temperature or the velocity [8,9,60–67] that the dynamics of turbulent RBC includes oscillations with a characteristic frequency that seems to be related to the turnover time of the LSC (see, however, [68,69]). One can use this frequency to determine Reynolds numbers Re_{ac}, Re_{sl}, or Re_{f_0} [see Eq. (9)]. It turns out that all three are equal to each other within experimental resolution; thus the three measurements may be regarded as alternative experimental methods to study the same phenomenon.

It is now known that the origin of these oscillations in RBC can be found, at least over a wide parameter range, in both a torsional and a sloshing mode of the LSC. The torsional mode is a time-periodic twist of the circulation plane of the LSC that consists, at a given moment, of a rotation in opposite azimuthal directions in the top and the bottom halves of the sample [70,71]. The sloshing mode is a periodic vertically and radially uniform lateral displacement of the circulation plane [72–74]. These two modes have the same frequency.

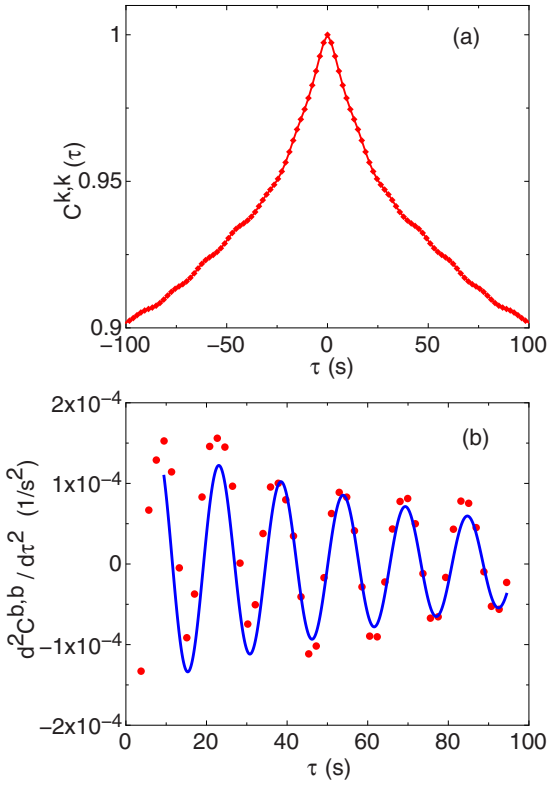

FIG. 15. (a) Azimuthally averaged autocorrelation function for the largest superheat $T_b - T_{on} = 10.4$ K and two-phase flow in cell A for $k = b$. (b) Points show the second derivative of the averaged autocorrelation function for $k = b$ in (a) with respect to τ. The line shows the fit of Eq. (23) to the data.

In our case of LHC we found that a well developed LSC extending as a single convection roll over the entire volume of a $\Gamma = 1$ sample does not seem to exist (see Sec. V B). Thus it would not have been surprising if local temperature oscillations also were absent. This, however, is not the case, and in the remainder of this section we report on such frequency measurements. Even though the results have common features with those for RBC, their interpretation in terms of a torsional and sloshing mode obviously has to be done with caution.

1. Reynolds numbers from correlation functions

In this section we present measurements of a frequency using the sidewall thermistors. We used the autocorrelation functions

$$\tilde{C}^{k,k}_{i,i}(\tau) = \langle [T_{k,i}(t) - \langle T_{k,i}\rangle] \times [T_{k,i}(t+\tau) - \langle T_{k,i}\rangle]\rangle \tag{21}$$

with the normalization

$$C^{k,k}_{i,i}(\tau) = \tilde{C}^{k,k}_{i,i}(\tau)/\tilde{C}^{k,k}_{i,i}(0) \tag{22}$$

calculated from the temperature time series $T_{k,i}(t)$ of the thermistors in the sidewall. They reveal an oscillatory signal very similar to that found in RBC [75]. The eight correlation functions corresponding to $i = 0, \ldots, 7$ at a given k can be averaged to yield $\bar{C}^{k,k}(\tau)$. An example from cell A is shown in Fig. 15(a). The data clearly reveal oscillations also for our case of LHC.

The oscillatory contribution to $\bar{C}^{k,k}(\tau)$ is weak and it is difficult to extract a reliable frequency directly from the data. As noted in Ref. [75], the oscillations become more obvious in the second

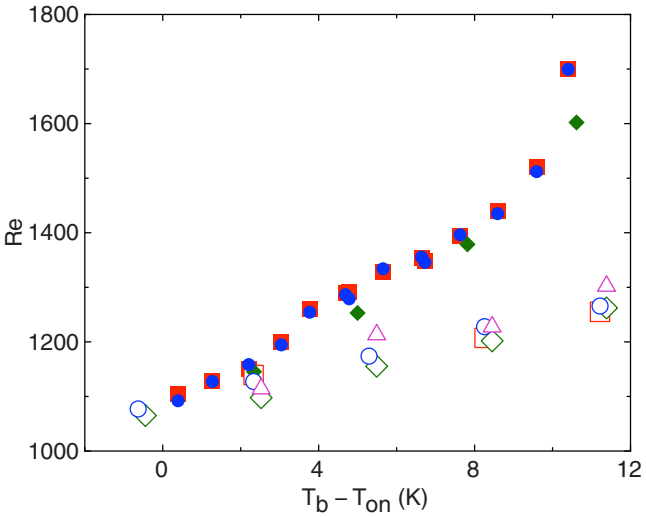

FIG. 16. Reynolds numbers as a function of the superheat $T_b - T_{on}$. Blue circles show Re_{ac} at the lower plane $k = b$ of cell A, red squares show Re_{sl} based on the sloshing-mode oscillations at the lower plane $k = b$ of cell A, green diamonds show Re_{f_0} from temperature oscillations in the interior of cell B, and purple triangles show Re_U for $\xi = 0.125$ and $\bar{z}/L = 0.50$ from Fig. 13(c). Open symbols show one-phase flow and closed symbols two-phase flow.

derivative of $\bar{C}^{k,k}(\tau)$. This is shown in Fig. 15(b). The function

$$d^2C/d\tau^2 = c_1 \exp(-\tau/\mathcal{T}^{bg}) \cos(2\pi\tau/\mathcal{T}^{ac}) \tag{23}$$

provides a reasonable fit and gives both the oscillation period $\mathcal{T}^{ac}$ and the exponential decay time $\mathcal{T}^{bg}$ of the oscillations. Using $\mathcal{T}^{ac}$, Re_{ac} is given by Eq. (9).

Results for Re_{ac} at the lower plane $k = b$ of cell A are shown in Fig. 16 as blue circles and as a function of the superheat. Results for $k = m$ and $k = t$ differ by less than 1% from the $k = b$ values and are not shown. The data indicate that Re_{ac} of one-phase flow (open symbols) is enhanced significantly by the bubbles of the two-phase flow (closed symbols). At the larger superheat values this enhancement reaches values up to about 25%. We note, however, that this is much smaller than the 60% enhancement found for the bubbles of Re_V (see Sec. V C 3 and Fig. 14).

2. *Reynolds numbers from the sloshing mode*

As discussed at the beginning of Sec. V D, the LSC in turbulent RBC undergoes both torsional oscillations and a periodic lateral displacement referred to as the sloshing mode. The antisymmetric sine terms in a Fourier decomposition of the eight sidewall temperatures at a given height can characterize the off-center displacement inherent in this mode [74]. The corresponding sinusoidal Fourier amplitudes are given by

$$D_n = \sum_{i=1}^{8} \{[T - T_0 - \delta \cos(\theta_i - \theta_0)] \sin[n(\theta_i - \theta_0)]\}. \tag{24}$$

The contribution $D_2 \neq 0$ corresponds to a temperature profile that is tilted in the azimuthal direction so that the temperature extrema, located at θ_h and θ_c, come closer together, corresponding to a slosh displacement. In the absence of a sloshing mode θ_h and θ_c are separated by π. Thus it is convenient to define the slosh displacement angle as $\theta' = (\theta_h - \theta_c - \pi)/2$. It satisfies the equation [74]

$$\delta \sin\theta' = 2D_2 \cos(2\theta'). \tag{25}$$

We calculated θ' only at the lower plane $k = b$ of cell A because we found no coherent azimuthal variation at the other levels (see Fig. 12). The power spectrum of θ' is shown in Fig. 17. In addition to

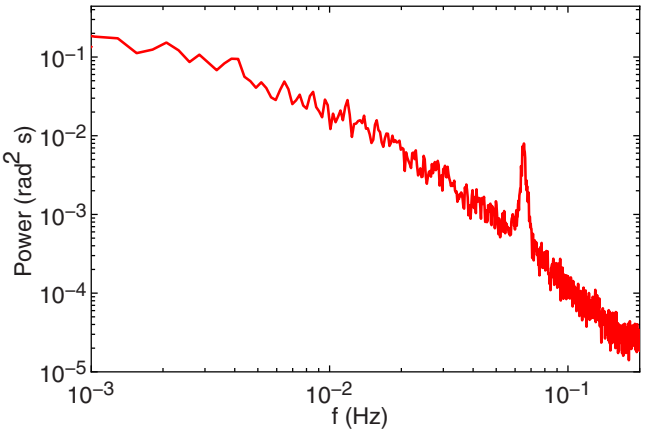

FIG. 17. Power-spectral density of the displacement angle θ' at the lower plane $k = b$ in cell A for two-phase flow at a superheat $T_b - T_{on} = 10.4$ K.

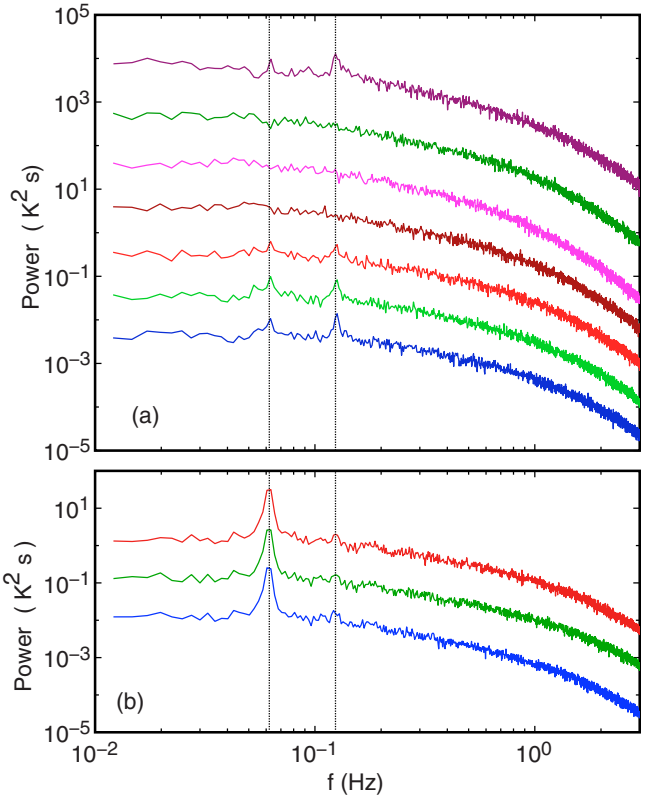

FIG. 18. Power spectra for cell A at the locations within the fluid given in Table I. These results are for two-phase flow and $T_b - T_{on} = 10.62$ K. (a) Spectra along the sample centerline ($\xi = 1.00$). (b) Spectra near the sidewall ($\xi = 0.125$). In both cases the lowest line (blue) is for the lowest thermistor at that radial location and the higher ones are successively shifted upward by a factor of 10. The vertical dotted lines correspond to $f_0 = 0.062$ Hz and $2f_0 = 0.124$ Hz.

a broad contribution due to the driving of the LSC dynamics by the turbulent background [14,43], it reveals a remarkably sharp peak at the sloshing frequency f_{sl}. A similar spectrum was obtained also from the time series for D_2 and yielded the same f_{sl}. The period $\mathcal{T}_{sl} = 1/f_{sl}$ was used with Eq. (9) to calculate Re_{sl}. The results are shown as red squares in Fig. 16. As expected from measurements for RBC, they agree very well with the results for Re_{ac} (see Sec. V D 1) that are shown as blue circles in the same figure.

3. Reynolds numbers from local temperature oscillations

The power spectra derived from the internal thermometers of cell B are shown in Fig. 18 for the largest superheat $T_b - T_{on} = 10.62$ K in two-phase flow. Spectra obtained for one-phase flow looked very similar. The spectra for the thermistors near the wall [$\xi = 0.125$, Fig. 18(b)] all show a strong peak at the same frequency $f_0 = 0.062$ Hz (left vertical dotted line) and a second weak peak at the second harmonic $2f_0 = 0.124$ Hz (right vertical dotted line). The peaks in the spectra on the cell axis [$\xi = 1.00$, Fig. 18(a)] are smaller, but still quite discernible for the thermistors close to the bottom and top plates. Near the sample center they are only barely visible.

The data show that there is a unique frequency $f_0 = 0.062$ Hz at all locations where the spectral peak can be identified. It is used to calculate the corresponding Reynolds number Re_{f_0} from Eq. (9). These results are shown as green diamonds in Fig. 16. They agree well with those for Re_{ac} and Re_{sl}, in the one-phase and two-phase states.

VI. CONCLUSION

We reported on measurements that characterize boiling in a cylindrical sample of fluid with $\mathrm{Pr} \simeq 8$ and aspect ration $\Gamma = 1.00$ heated from below. The sample geometry was the same as that of NG, except that we installed nine internal thermometers for local temperature measurements in one sample (cell B, Sec. III C) and 24 thermometers mounted in the sidewall of another (cell A, Sec. III B); NG only had two internal devices. The additional thermometers made it possible to measure temperature-oscillation frequencies, as well as Reynolds numbers using temperature correlation functions and the EM of He and Zhang [31]. Only a central circular area of 2.54 cm diameter of the bottom plate (of 8.83 cm diameter) was heated and was covered by a lattice of controlled bubble-nucleation centers. This geometry differs from RBC where the entire bottom plate is heated; we refer to it as locally heated convection.

Heat-transport measurements were made in both one-phase and two-phase flow. They yielded Nusselt numbers that agreed with those of NG, thus indicating that global properties were not changed much by the insertion of additional thermometers.

Using the sidewall thermometers, we studied the large-scale flow in the turbulent system. The LSF did not consist of a single well-developed convection roll as in RBC. In the bottom portion of the sample there was a flow structure that yielded a dominating sinusoidal azimuthal temperature variation as in RBC. This sinusoidal mode was stronger for two-phase flow than for one-phase flow, but in both cases weaker than for RBC. At the midplane and in the top portion this mode did not dominate and higher Fourier modes contained more energy. This finding indicates a mean-flow structure that is much more complex and disordered than the single-roll mean flow in RBC.

We measured temperature cross-correlation functions (CCFs) using temperature probes separated vertically by up to 12 mm. They were used to determine both mean-flow velocities U and fluctuation velocities V [31,33–35] using the EA of He and co-workers [31,36]. The applicability of the EA to our system is supported by the agreement of our results with several general results of the EA [Eqs. (11)–(13)]. They yielded internally consistent results and fluctuation Reynolds numbers that agree within 10% or so with those measured by other means for RBC (see Sec. V C 2).

We found that the EA predictions were valid even in cases where the maximum value of the CCF $C(\delta z, \tau)$ was as small as 0.2 or so. One would not expect *a priori* that the elliptic approximation, a second-order series expansion of $C(\delta z, \tau)$ about $C(0,0) = 1$, would be valid in such a case. Our result

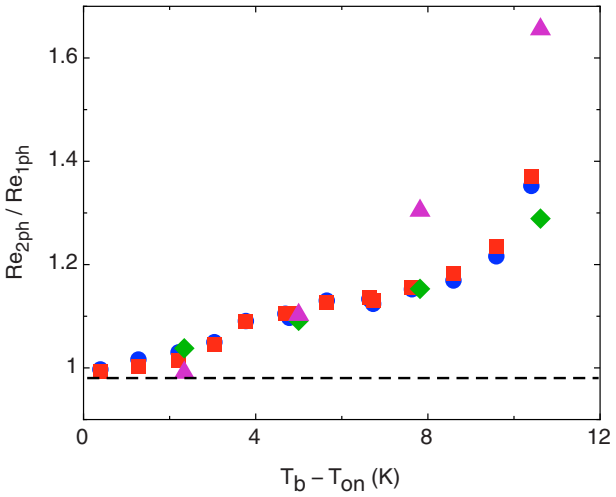

FIG. 19. Relative increase of Reynolds numbers in two-phase flow compared to one-phase flow as a function of the superheat. Blue circles show Re_{ac}, green diamonds Re_{f_0}, red squares Re_{sl}, and purple triangles Re_V for $\bar{z}/L = 0.25$ and $\xi = 1.00$ from Fig. 14.

supports the relevance also for thermally driven convection of the assertion by He and co-workers [31,36], based on the Kolmogorov similarity hypothesis, that the results of the EA should be valid for all time and space displacements within the inertial range. Indeed, we showed that all our values of δz and τ were within the inertial range of our measured fluctuation spectra.

We saw that three methods of determining Reynolds numbers from frequency measurements (Re_{ac}, Re_{sl}, and Re_{f_0}) all give the same results within our resolution, both in one-phase and in two-phase flow. This strongly suggests that the measured frequencies have the same origin, as they are believed to have in RBC. In RBC we would argue that they all come from the synchronous torsional and sloshing modes of the LSC, but in our case of LHC we found that a well developed large-scale flow does not exist. Thus the agreement between the three Reynolds numbers is remarkable and its origin needs further elucidation.

The comparison of the frequency-based Reynolds numbers with those derived from the velocities obtained from the elliptic model is more complex. Since in RBC the frequencies are believed to correspond to an inverse turnover time of the LSC, the comparison should be made with Re_U rather than Re_V. However, since U varies strongly with position within the sample, its maximum value near (but not too near) the sidewall should be used. Based on this consideration, we made the comparison using Re_U of one-phase flow at $\bar{z}/L = 0.50$ and $\xi = 0.125$ (Fig. 16). There was good agreement between Re_U and the frequency-based Re. This agreement is somewhat surprising because U depends on the LSF structure and orientation. As discussed above, the LSF structure of LHC is not the same as that of RBC.

For all three frequency-based Re the same enhancement due to the bubbles of two-phase flow was found (Fig. 19); it reached values near 20% or 30% at the largest superheats. Any enhancement of Re_U due to the bubbles is not meaningful since in addition to any direct flow-speed enhancement the bubbles of two-phase flow also alter the LSF structure and orientation and thereby indirectly change U. The enhancement of Re_V (Figs. 14 and 19) at the larger superheats is larger than that of the frequency-based Re and reaches values in excess of 60%. This effect is consistent with direct numerical simulations with bubble injection [56–59].

ACKNOWLEDGMENTS

This work was supported by the U.S. National Science Foundation through Grant No. DMR11-58514, by the Netherlands Center for Multiscale Catalytic Energy Conversion (MCEC), an NWO

Gravitation program funded by the Ministry of Education, Culture and Science of the government of the Netherlands, and by Natural Science Foundation of China under Grant No. 11672156.

[1] L. P. Kadanoff, Turbulent heat flow: Structures and scaling, Phys. Today **54**(8), 34 (2001).
[2] G. Ahlers, Turbulent convection, Physics **2**, 74 (2009).
[3] G. Ahlers, S. Grossmann, and D. Lohse, Heat transfer and large scale dynamics in turbulent Rayleigh-Bénard convection, Rev. Mod. Phys. **81**, 503 (2009).
[4] D. Lohse and K.-Q. Xia, Small-scale properties of turbulent Rayleigh-Bénard convection, Annu. Rev. Fluid Mech. **42**, 335 (2010).
[5] F. Chillà and J. Schumacher, New perspectives in turbulent Rayleigh-Bénard convection, Eur. Phys. J. E **35**, 58 (2012).
[6] M. Sano, X. Z. Wu, and A. Libchaber, Turbulence in helium-gas free convection, Phys. Rev. A **40**, 6421 (1989).
[7] R. Verzicco and R. Camussi, Prandtl number effects in convective turbulence, J. Fluid Mech. **383**, 55 (1999).
[8] X. L. Qiu and P. Tong, Large scale velocity structures in turbulent thermal convection, Phys. Rev. E **64**, 036304 (2001).
[9] X. L. Qiu, X. D. Shang, P. Tong, and K.-Q. Xia, Velocity oscillations in turbulent Rayleigh-Bénard convection, Phys. Fluids **16**, 412 (2004).
[10] C. Sun, K. Q. Xia, and P. Tong, Three-dimensional flow structures and dynamics of turbulent thermal convection in a cylindrical cell, Phys. Rev. E **72**, 026302 (2005).
[11] E. Brown, A. Nikolaenko, and G. Ahlers, Reorientation of the Large-Scale Circulation in Turbulent Rayleigh-Bénard Convection, Phys. Rev. Lett. **95**, 084503 (2005).
[12] C. Sun, H. D. Xi, and K. Q. Xia, Azimuthal Symmetry, Flow Dynamics, and Heat Transport in Turbulent Thermal Convection in a Cylinder with an Aspect Ratio of 0.5, Phys. Rev. Lett. **95**, 074502 (2005).
[13] E. Brown and G. Ahlers, Rotations and cessations of the large-scale circulation in turbulent Rayleigh-Bénard convection, J. Fluid Mech. **568**, 351 (2006).
[14] E. Brown and G. Ahlers, A model of diffusion in a potential well for the dynamics of the large-scale circulation in turbulent Rayleigh-Bénard convection, Phys. Fluids **20**, 075101 (2008).
[15] X. He, E. Bodenschatz, and G. Ahlers, Azimuthal diffusion of the large-scale-circulation plane, and absence of significant non-Boussinesq effects, in turbulent convection near the ultimate-state transition, J. Fluid Mech. **791**, R3 (2016).
[16] A. Tilgner, A. Belmonte, and A. Libchaber, Temperature and velocity profiles of turbulence convection in water, Phys. Rev. E **47**, R2253 (1993).
[17] S. L. Lui and K.-Q. Xia, Spatial structure of the thermal boundary layer in turbulent convection, Phys. Rev. E **57**, 5494 (1998).
[18] J. Wang and K.-Q. Xia, Spatial variations of the mean and statistical quantities in the thermal boundary layers of turbulent convection, Eur. Phys. J. B **32**, 127 (2003).
[19] E. Brown and G. Ahlers, Temperature gradients, and search for non-Boussinesq effects, in the interior of turbulent Rayleigh-Bénard convection, Europhys. Lett. **80**, 14001 (2007).
[20] G. Ahlers, E. Bodenschatz, D. Funfschilling, S. Grossmann, X. He, D. Lohse, R. Stevens, and R. Verzicco, Logarithmic Temperature Profiles in Turbulent Rayleigh-Bénard Convection, Phys. Rev. Lett. **109**, 114501 (2012).
[21] G. Ahlers, E. Bodenschatz, and X. He, Logarithmic temperature profiles of turbulent Rayleigh-Bénard convection in the classical and ultimate state for a Prandtl number of 0.8, J. Fluid Mech. **758**, 436 (2014).
[22] P. Wei and G. Ahlers, Logarithmic temperature profiles in the bulk of turbulent Rayleigh-Bénard convection for a Prandtl number of 12.3, J. Fluid Mech. **758**, 809 (2014).
[23] M. V. R. Malkus, The heat transport and spectrum of thermal turbulence, Proc. R. Soc. London Ser. A **225**, 196 (1954).
[24] C. H. B. Priestley, Convection from a large horizontal surface, Aust. J. Phys. **7**, 176 (1954).

[25] C. H. B. Priestley, *Turbulent Transfer in the Lower Atmosphere* (University of Chicago Press, Chicago, 1959).
[26] E. A. Spiegel, Convection in stars, Annu. Rev. Astron. Astrophys. **9**, 323 (1971).
[27] C. Sun, Y.-H. Cheung, and K.-Q. Xia, Experimental studies of the viscous boundary layer properties in turbulent Rayleigh-Bénard convection, J. Fluid Mech. **605**, 79 (2008).
[28] J.-Q. Zhong, D. Funfschilling, and G. Ahlers, Enhanced Heat Transport by Turbulent Two-Phase Rayleigh-Bénard Convection, Phys. Rev. Lett. **102**, 124501 (2009).
[29] D. Narezo Guzman, Y. Xie, S. Chen, D. Fernandez-Rivas, C. Sun, D. Lohse, and G. Ahlers, Heat-flux enhancement by vapour-bubble nucleation in Rayleigh-Bénard turbulence, J. Fluid Mech. **787**, 331 (2015).
[30] D. Narezo Guzman, T. Fraczek, C. Reetz, C. Sun, D. Lohse, and G. Ahlers, Vapour-bubble nucleation and dynamics in turbulent Rayleigh-Bénard convection, J. Fluid Mech. **795**, 60 (2016).
[31] G.-W. He and J.-B. Zhang, Elliptic model for space-time correlations in turbulent shear flows, Phys. Rev. E **73**, 055303(R) (2006).
[32] G. He, G. Jin, and Y. Yang, Space-time correlations and dynamic coupling in turbulent flows, Annu. Rev. Fluid Mech. **49**, 51 (2016).
[33] C. Sun, Q. Zhou, and K.-Q. Xia, Cascades of Velocity and Temperature Fluctuations in Buoyancy-Driven Thermal Turbulence, Phys. Rev. Lett. **97**, 144504 (2006).
[34] X. He, E. Ching, and P. Tong, Locally averaged thermal dissipation rate in turbulent thermal convection: A decomposition into contributions from different temperature gradient components, Phys. Fluids **23**, 025106 (2011).
[35] X. He, X. Shang, and P. Tong, Test of the anomalous scaling of passive temperature fluctuations in turbulent Rayleigh-Bénard convection with spatial inhomogeneity, J. Fluid Mech. **753**, 104 (2014).
[36] X. Zhao and G.-W. He, Space-time correlations of fluctuating velocities in turbulent shear flows, Phys. Rev. E **79**, 046316 (2009).
[37] X. He, G. He, and P. Tong, Small-scale turbulent fluctuations beyond Taylor's frozen-flow hypothesis, Phys. Rev. E **81**, 065303 (2010).
[38] X. He and P. Tong, Kraichnan random sweeping hypothesis in homogeneous turbulent convection, Phys. Rev. E **83**, 037302 (2011).
[39] A. Oberbeck, Über die Wärmeleitung der Flüssigkeiten bei Berücksichtigung der Strömungen infolge von Temperaturdifferenzen, Ann. Phys. Chem. **243**, 271 (1879).
[40] J. Boussinesq, *Theorie Analytique de la Chaleur* (Gauthier-Villars, Paris, 1903), Vol. 2.
[41] S. Lam, X. D. Shang, S. Q. Zhou, and K.-Q. Xia, Prandtl-number dependence of the viscous boundary layer and the Reynolds-number in Rayleigh-Bénard convection, Phys. Rev. E **65**, 066306 (2002).
[42] X. He, D. van Gils, E. Bodenschatz, and G. Ahlers, Reynolds numbers and the elliptic approximation near the ultimate state of turbulent Rayleigh-Bénard convection, New J. Phys. **17**, 063028 (2015).
[43] E. Brown and G. Ahlers, Large-Scale Circulation Model of Turbulent Rayleigh-Bénard Convection, Phys. Rev. Lett. **98**, 134501 (2007).
[44] S. B. Pope, *Turbulent Flow* (Cambridge University Press, Cambridge, 2000).
[45] X. He, D. van Gils, E. Bodenschatz, and G. Ahlers, Logarithmic Spatial Variations and Universal f^{-1} Power Spectra of Temperature Fluctuations in Turbulent Rayleigh-Bénard Convection, Phys. Rev. Lett. **112**, 174501 (2014).
[46] A. M. Obukhov, Structure of the temperature field in a turbulent flow, Izv. Akad. Nauk SSSR Ser. Geog. Geofiz. **13**, 58 (1949).
[47] S. Corrsin, On the spectrum of isotropic temperature fluctuations in an isotropic turbulence, J. Appl. Phys. **22**, 469 (1951).
[48] R. Bolgiano, Turbulent spectra in a stably stratified atmosphere, J. Geophys. Res. **64**, 2226 (1959).
[49] A. M. Obukhov, On the influence of Archimedean forces on the structure of the temperature field in a turbulent flow, Dokl. Akad. Nauk. SSR **125**, 1246 (1959).
[50] Q. Zhou, C.-M. Li, Z.-M. Lu, and Y.-L. Liu, Experimental investigation of longitudinal space-time correlations of the velocity field in turbulent Rayleigh-Bénard convection, J. Fluid Mech. **683**, 94 (2011).
[51] J. Hogg and G. Ahlers, Reynolds-number measurements for low-Prandtl-number turbulent convection of large aspect-ratio samples, J. Fluid Mech. **725**, 664 (2013).

[52] P. Wei and G. Ahlers, On the nature of fluctuations in turbulent Rayleigh-Bénard convection at large Prandtl numbers, J. Fluid Mech. **802**, 203 (2016).
[53] R. P. J. Kunnen, H. J. H. Clercx, and B. J. Geurts, Breakdown of large-scale circulation in turbulent rotating convection, Europhys. Lett. **84**, 24001 (2008).
[54] R. J. Stevens, H. J. Clercx, and D. Lohse, Effect of plumes on measuring the large scale circulation, Phys. Fluids **23**, 095110 (2011).
[55] S. Weiss and G. Ahlers, Heat transport by turbulent rotating Rayleigh-Bénard convection, J. Fluid Mech. **684**, 407 (2011).
[56] R. Lakkaraju, L. Schmidt, P. Oresta, F. Toschi, R. Verzicco, D. Lohse, and A. Prosperetti, Effect of vapor bubbles on velocity fluctuations and dissipation rates in bubble Rayleigh-Bénard convection, Phys. Rev. E **84**, 036312 (2011).
[57] L. Biferale, P. Perlekar, M. Sbragaglia, and F. Toschi, Convection in Multiphase Fluid Flows Using Lattice Boltzmann Methods, Phys. Rev. Lett. **108**, 104502 (2012).
[58] R. Lakkaraju, R. Stevens, P. Oresta, R. Verzicco, D. Lohse, and A. Prosperetti, Heat transport in bubbling turbulent convection, Proc. Natl. Acad. Sci. USA **110**, 9237 (2013).
[59] R. Lakkaraju, F. Toschi, and D. Lohse, Bubbling reduces intermittency in turbulent thermal convection, J. Fluid Mech. **745**, 1 (2014).
[60] F. Heslot, B. Castaing, and A. Libchaber, Transition to turbulence in helium gas, Phys. Rev. A **36**, 5870 (1987).
[61] B. Castaing, G. Gunaratne, F. Heslot, L. Kadanoff, A. Libchaber, S. Thomae, X. Z. Wu, S. Zaleski, and G. Zanetti, Scaling of hard thermal turbulence in Rayleigh-Bénard convection, J. Fluid Mech. **204**, 1 (1989).
[62] S. Ciliberto, S. Cioni, and C. Laroche, Large-scale flow properties of turbulent thermal convection, Phys. Rev. E **54**, R5901 (1996).
[63] T. Takeshita, T. Segawa, J. A. Glazier, and M. Sano, Thermal Turbulence in Mercury, Phys. Rev. Lett. **76**, 1465 (1996).
[64] S. Cioni, S. Ciliberto, and J. Sommeria, Strongly turbulent Rayleigh-Bénard convection in mercury: Comparison with results at moderate Prandtl number, J. Fluid Mech. **335**, 111 (1997).
[65] X. L. Qiu and P. Tong, Onset of Coherent Oscillations in Turbulent Rayleigh-Bénard Convection, Phys. Rev. Lett. **87**, 094501 (2001).
[66] J. J. Niemela, L. Skrbek, K. R. Sreenivasan, and R. J. Donnelly, The wind in confined thermal turbulence, J. Fluid Mech. **449**, 169 (2001).
[67] X. L. Qiu and P. Tong, Temperature oscillations in turbulent Rayleigh-Bénard convection, Phys. Rev. E **66**, 026308 (2002).
[68] E. Brown, D. Funfschilling, and G. Ahlers, Anomalous Reynolds-number scaling in turbulent Rayleigh-Bénard convection, J. Stat. Mech. (2007) P10005.
[69] K.-Q. Xia, Two clocks for a single engine in turbulent convection, J. Stat. Mech. (2007) N11001.
[70] D. Funfschilling and G. Ahlers, Plume Motion and Large Scale Circulation in a Cylindrical Rayleigh-Bénard Cell, Phys. Rev. Lett. **92**, 194502 (2004).
[71] D. Funfschilling, E. Brown, and G. Ahlers, Torsional oscillations of the large-scale circulation in turbulent Rayleigh-Bénard convection, J. Fluid Mech. **607**, 119 (2008).
[72] H.-D. Xi, S.-Q. Zhou, Q. Zhou, T.-S. Chan, and K.-Q. Xia, Origin of the Temperature Oscillation in Turbulent Thermal Convection, Phys. Rev. Lett. **102**, 044503 (2009).
[73] Q. Zhou, H.-D. Xi, S.-Q. Zhou, C. Sun, and K.-Q. Xia, Oscillations of the large-scale circulation in turbulent Rayleigh-Bénard convection: the sloshing mode and its relationship with the torsional mode, J. Fluid Mech. **630**, 367 (2009).
[74] E. Brown and G. Ahlers, The origin of oscillations of the large-scale circulation of turbulent Rayleigh-Bénard convection, J. Fluid Mech. **638**, 383 (2009).
[75] J.-Q. Zhong and G. Ahlers, Heat transport and the large-scale circulation in rotating turbulent Rayleigh-Bénard convection, J. Fluid Mech. **665**, 300 (2010).